PHYSICAL REVIEW C VOLUME 19, NUMBER 3 MARCH 1979

Charged-particle spectra: 90 MeV protons on ^{27}Al, ^{58}Ni, ^{90}Zr, and ^{209}Bi

J. R. Wu, C. C. Chang, and H. D. Holmgren

Department of Physics and Astronomy, University of Maryland College Park, Maryland

(Received 13 March 1978)

Complete charged light-particle ($Z \leq 2$, $A \leq 4$) energy spectra were measured for 90 MeV protons on ^{27}Al, ^{58}Ni, ^{90}Zr, and ^{209}Bi and 100 MeV protons on ^{58}Ni. The energy spectra show a strong angular dependence and the spectral shapes at a given angle for the same particle type are similar in the high-energy continuum for all target nuclei. The non-equilibrium, charged light-particle yields show an $A^{1/3}$ dependence and are approximately given by $(200 \pm 10)A^{1/3}$(mb). One striking feature is the similarity of the shapes of the p, d, and t spectra, if the spectra are shifted by an appropriate binding energy. The relative intensity is approximately $p{:}d{:}t$ 1:1/10:1/100 at all angles. In the backward directions ($\theta \geq 140°$) the spectra exhibit characteristic evaporation behavior with approximately the same slope for each target nucleus for a given observed particle. The slopes of the evaporation peaks (corresponding to a temperature of 2–3 MeV) for the different particle type are also rather similar. The experimental results were analyzed within the framework of the pre-equilibrium exciton model together with the evaporation theory. The pre-equilibrium exciton model using a 2p-1h initial configuration generally reproduces the experimental angle-integrated energy spectra reasonably well in shape, but underestimates especially the proton yield in the region of high-energy continuums.

[NUCLEAR REACTION: ^{27}Al, ^{58}Ni, ^{90}Zr, ^{209}Bi (p, xp), (p, xd), (p, xt), $(p, x^3\text{He})$, $(p, x\alpha)$, $E_p = 90$ MeV; $\theta_L = 20°–40°$, ^{58}Ni (p, xp), (p, xd), (p, xt), $(p, x^3\text{He})$, $(p, x\alpha)$, $E_p = 100$ MeV; $\theta_L = 15°–155°$, measured $d^2\sigma/d\Omega d\epsilon$, deduced $d\sigma/d\epsilon$ and $\sigma(E)$. Comparisons with preequilibrium exciton and evaporation models.]

I. INTRODUCTION

We have previously reported studies of charged light-particle ($Z \leq 2, A \leq 4$) energy spectra resulting from medium-energy deuteron[1] and α-particle[2] induced reactions. A number of interesting features have emerged from these studies. From the analyses of these results it was concluded that in addition to the direct one-step processes secondary interaction processes (multiple collisions) are important. The cross sections leading to bound states of the residual nucleus constitute only a small fraction of the total reaction cross sections. Particles in the high-energy continuum appear to result mainly from interactions involving only a few nucleons of the target nucleus. The low-energy particles are due either to the compound nucleus evaporation or to the higher order preequilibrium decay. The projectile breakup process was found to be significant for composite projectiles.[1,2] The basic reaction mechanisms involved in reactions induced by different composite projectiles with energies around 100 MeV appear to be similar.

The energy spectra of charged light particle from proton induced reactions have been widely studied. Most of these measurements were performed at lower energies ($\lesssim 60$ MeV).[3] Limited data are available at higher energies.[4] It is generally believed that the single collision processes (quasifree scattering) are the predominant interactions in the energy range of several hundred MeV and that multiple collision processes dominate in the neighborhood of ~100 MeV. In the last few years a number of experiments have been carried out to study the nuclear structure and the reaction mechanisms by means of reactions such as $(p, 2p)$, $(p, p\alpha)$, (p, pd), and $(p, d^3\text{He})$ using 100 MeV protons.[5] In-beam γ-ray measurements have also been used to identify the product nuclei resulting from reactions induced by 100 MeV protons.[6] In order to obtain a more complete picture of the reaction mechanisms involved in this energy region we have measured the complete spectra of charged light particles produced by 90 MeV protons on four target nuclei spanning the periodic table (the same targets were used in the studies of deuteron and α-particle induced reactions) and by 100 MeV protons on ^{58}Ni. Some of the 100 MeV results have been previously reported.[7]

Data for 62 MeV protons reported by Bertrand and Peele[3] show that the particle yields from these reactions are governed by peripheral type of collisions. This conclusion is based on the fact that the nonequilibrium yield has an approximate $A^{1/3}$ dependence. Processes which involve the emission of particles after several interactions and from the equilibrated nucleus in the compound stage were also observed. These lower energies data have been interpreted in terms of various reaction models.[3,8]

In Sec. III, the experimental results are given and are compared with data at lower energies. The comparisons of the experimental results with the pre-equilibrium exciton model and the conventional evaporation model are given in Sec. IV.

II. EXPERIMENTAL METHOD

In this series of experiments, protons accelerated to 90 and 100 MeV by the University of Maryland Cyclotron were used to bombard ^{27}Al (1.72 mg/cm^2), ^{58}Ni (1.11 mg/cm^2 for 90 MeV protons and 1.6 mg/cm^2 for 100 MeV protons), ^{90}Zr (5.8 mg/cm^2), and ^{209}Bi (8.85 mg/cm^2) targets. The primary interest of this experiment was to measure the charged light-particle ($Z \leq 2, A \leq 4$) energy spectra over the entire energy range of particles produced by 90 MeV protons on the above targets. Two triple-counter telescopes were employed to compensate for the gaps which appeared in the spectrum due to detector dead layers and electronic thresholds in each telescope. The detector arrangements of these two triple-counter telescopes were (1) 100 μm (Si)–1000 μm (Si)–7.6 cm NaI, and (2) 500 μm (Si)–4000 μm (Si-Li)-500 μm (Si). The detector solid angles were 0.271 and 0.165 msr, respectively. The details of the experimental methods, including data collection, reduction, computer programs, and the error analyses were described in Refs. 1 and 9. The overall uncertainties for the experimental data are approximately 10%.

The experimental laboratory differential cross sections were transformed to the c.m. system using the relationship

$$\frac{1}{p'}\frac{d^2\sigma'(\theta')}{d\Omega' d\epsilon'}=\frac{1}{p}\frac{d^2\sigma(\theta)}{d\Omega d\epsilon},$$

where p and p' are the momenta of the emitted particles in the laboratory and the c.m. systems, respectively. In carrying out the point by point transformation, the assumption was made that all observed particles were emitted from a nucleus moving with initial c.m. velocity.

The cross sections integrated over either laboratory or c.m. angles, $d\sigma/d\epsilon = 2\pi\int_0^\pi (d^2\sigma/d\Omega d\epsilon)\sin\theta d\theta$, were obtained by means of Gauss integration. For integration purposes, the Lagrange interpolation/extrapolation method was employed to estimate the cross section of those integration points which fall outside of the experimental data.

III. EXPERIMENTAL RESULTS AND DISCUSSION

The spectra of charged light particle were measured for the four target nuclei over the energy range from ~2 MeV up to the maximum possible energy and the angular range from 20° to 140°. Data with limited energy and angular ranges for 100 MeV protons on ^{58}Ni were also obtained. Table I summarizes the experimental conditions and some of the results. The results of some earlier work performed at another laboratory at lower energies are listed in Table II.[3]

Figure 1 displays the laboratory differential energy spectra for p, d, t, ^{3}He and α particles for 90 MeV proton induced reactions on ^{27}Al, ^{58}Ni, ^{90}Zr, and ^{209}Bi. Spectra for the ^{58}Ni(p,x) reaction $E_p=100$ MeV are shown in Fig. 2. The characteristic behavior of these spectra is quite similar to those observed for the deuteron[1] and α-particle[2] induced reactions. The spectra vary rapidly with angle in the forward direction and remain more constant in shape and magnitude in the backward direction (> 90°). The high-energy particles are produced mainly at forward angles for all target nuclei. On the other hand, the low-energy particles are nearly isotropic for lighter nuclei and are slightly forward peaked for heavy nuclei. The typical angular distributions in the c.m. frame for various energy bins are shown in Fig. 3 for the ^{58}Ni(p,x) reactions $E_p=90$ MeV.

The spectra for the ^{58}Ni(p,x) reactions at $\theta_L=20°$ in the laboratory system are shown in Fig. 4 to illustrate the general forward angle features of these data for each emitted particle. In the proton spectrum, a broad peak at $E_x \sim 63A^{-1/3}$ MeV corresponding to the excitation of the giant quadrupole resonance is observed. The laboratory angle-integrated spectra are also shown in Fig. 4. All spectra are plotted on the same scale to facilitate the comparison of their relative intensities. At forward angles the proton and deuteron spectra are very similar in shape and are almost flat in the region of continuum above the low-energy evaporation peak. The triton and ^{3}He spectra also show a similar behavior except that they exhibit a slight decrease with energy. The α-particle spectrum, however, decreases rapidly with energy. These observations suggest that the emission of nonequilibrium protons and deuterons result from a very similar process. The processes which result in the emission of tritons and ^{3}He may also be closely related, but the emission of α particles is clearly more complex.

Figure 5 shows the comparison of deuteron and triton spectra with those of protons for the ^{58}Ni(p,x) reactions at $E_p=100$ MeV. The deuteron

TABLE I. Summary of experimental conditions and measured integral cross sections.

Target and incident energy	Compound nucleus and initial excitation energy	Angles observed (degree)	Particle emitted	Low energy cutoff (MeV)	Reaction Q value (MeV)	Measured averaged emitted energy $\bar{E}$ (MeV)	Average low energy peak location (MeV)	Calculated Coulomb barrier[a] (MeV)	Measured integral cross section in laboratory[b] σ_t (mb)
^{27}Al	^{28}Si	20,30,	p	2.5	0	42.28	3.45	3.12	
E_p=90 MeV	E^*=98.33 MeV	45,60,	d	2.5	−10.83	28.04	3.45	2.96	999 ± 100
		75,90,	t	5.5	−15.92	22.92	···	2.86	
		105,120,	^{3}He	11.5	−11.65	29.11	···	5.28	
		140	^{4}He	2.5	1.61	8.49	4.45	5.15	
^{58}Ni	^{59}Cu	20,30,	p	1.5	0	23.01	4.55	5.52	
E_p=90 MeV	E^*=91.87 MeV	45,60,	d	3.5	−9.98	31.32	5.55	5.26	2186 ± 220
		75,90,	t	5.5	−13.97	26.01	···	5.10	
		105,120,	^{3}He	12.5	−11.84	30.78	···	9.84	
		140	^{4}He	3.5	−1.35	11.79	8.55	9.62	
^{90}Zr	^{91}Nb	20,30,	p	2.5	0	31.52	5.45	7.01	
E_p=90 MeV	E^*= 94.26 MeV	45,60,	d	2.5	−9.78	31.31	7.45	6.71	1768 ± 180
		75,90,	t	5.5	−12.66	24.55	7.45	6.52	
		105,120,	^{3}He	11.5	−12.14	30.05	13.45	12.71	
		140	^{4}He	4.5	−0.75	14.95	11.45	12.44	
^{209}Bi	^{210}Po	20,30,	p	4.5	0	58.24	18.55	11.49	
E_p=90 MeV	E^*= 94.54 MeV	45,60,	d	5.5	−5.23	37.94	16.55	11.09	1588 ± 160
		75,90,	t	5.5	−5.83	29.20	14.55	10.83	
		105,120,	^{3}He	12.5	−3.45	41.31	25.55	21.40	
		140	^{4}He	13.5	10.39	28.69	19.55	21.01	
^{58}Ni	^{59}Cu	15,25,	p	12.5	0	···	···	5.52	
E_p=100 MeV	E^*= 101.7 MeV	35,45,	d	16.5	−9.98	···	···	5.26	1127 ± 110
		60,80,	t	19.5	−13.97	···	···	5.10	
		100,130,	^{3}He	8.5[c]	−11.84	···	···	9.84	
		155	^{4}He	8.5[c]	−1.35	···	···	9.62	

[a] Coulomb barriers are calculated from $V_c = 1.44\, zZ/1.5(A^{1/3} + a^{1/3})$.

[b] Excluding the elastic scattering.

[c] For ^{58}Ni(p, $x\,^3$He) and ^{58}Ni(p, $x\alpha$) at E_p=100 MeV, ^{3}He particles are measured from 8.5 to 45.5 MeV.

TABLE II. Summary of experimental results of Ref. 3.

Target and incident energy	σ_t (mb)	σ_R (mb)	$Y=\sigma_t/\sigma_R$	Emitted particle	σ_β (mb)	σ_β/σ_t	$Y_\beta=\sigma_\beta/\sigma_R$
^{12}C 61 MeV	600.6	322	1.865	p	346.0	0.576	1.075
				d	71.1	0.118	0.221
				t	9.3	0.015	0.029
				^{3}He	18.2	0.030	0.057
				^{4}He	156.0	0.260	0.484
^{16}O 61 MeV	696.6	386	1.805	p	448.0	0.643	1.161
				d	78.7	0.113	0.204
				t	7.4	0.011	0.019
				^{3}He	14.5	0.021	0.038
				^{4}He	148.0	0.212	0.383
^{27}Al 62 MeV	979.22	537	1.824	p	705.6	0.721	1.314
				d	88.7	0.091	0.165
				t	8.88	0.009	0.017
				^{3}He	11.04	0.011	0.021
				^{4}He	165.0	0.168	0.307
^{54}Fe 62 MeV	1923.27	822	2.340	p	1670.0	0.868	2.032
				d	87.3	0.045	0.106
				t	6.92	0.004	0.008
				^{3}He	9.55	0.005	0.012
				^{4}He	149.5	0.078	0.182
^{54}Fe 39 MeV	1727.59	918	1.882	p	1542.0	0.893	1.680
				d	54.5	0.032	0.059
				t	2.69	0.002	0.003
				^{3}He	7.7	0.004	0.008
				^{4}He	120.7	0.070	0.131
^{54}Fe 29 MeV	1540.95	973	1.584	p	1409.0	0.914	1.448
				d	34.7	0.023	0.036
				t	0.93	0.001	0.001
				^{3}He	0.42	0.0003	0.0004
				^{4}He	95.9	0.062	0.099
^{89}Y 62 MeV	1064.2	1125	0.946	p	868.7	0.816	0.772
				d	78.4	0.074	0.070
				t	12.6	0.012	0.011
				^{3}He	4.0	0.004	0.004
				^{4}He	100.5	0.094	0.089
^{120}Sn 62 MeV	996.24	1349	0.739	p	811.0	0.814	0.601
				d	95.1	0.095	0.070
				t	23.6	0.024	0.017
				^{3}He	3.34	0.003	0.002
				^{4}He	63.2	0.063	0.047
^{197}Au 62 MeV	796.2	1799	0.443	p	654.6	0.822	0.364
				d	86.0	0.108	0.048
				t	21.3	0.027	0.012
				^{3}He	2.3	0.003	0.001
				^{4}He	32.0	0.040	0.018
^{209}Bi 62 MeV	864.08	1876	0.461	p	707.0	0.818	0.377
				d	95.0	0.110	0.051
				t	27.2	0.031	0.015
				^{3}He	2.58	0.003	0.001
				^{4}He	32.3	0.038	0.017

σ_t: Total integral charged particle yield.
σ_R: Total reaction cross section.
Y: Mean particle yield.
σ_β: Integral yield for particle β.

and triton spectra have been shifted by an appropriate binding energy and were scaled by a factor of 10 and 100, respectively. The similarity in spectral shape is obvious.

Figure 6(a) shows typical energy spectra observed at backward angle in the laboratory system for the ^{58}Ni(p,x) reactions at $\theta_L = 140°$ and $E_p = 90$ MeV. The α-particle and deuteron spectra have been multiplied by a factor of 10 and the triton spectrum by 100. Clearly the dominant channels are the protons and the α particles. The spectra for all particles have similar shapes. The proton spectrum, however, shows a change in slope starting at about 15 MeV. Figure 6(b) shows the laboratory and c.m. α-particle energy spectra for various target nuclei in the backward direction. It is interesting to note that the slope, corresponding to a temperature of 2–3 MeV, is nearly identical for all target nuclei. This suggests that particles emitted in the backward angles result from the same reaction mechanism.

Figure 7 demonstrates the A dependence of emit-

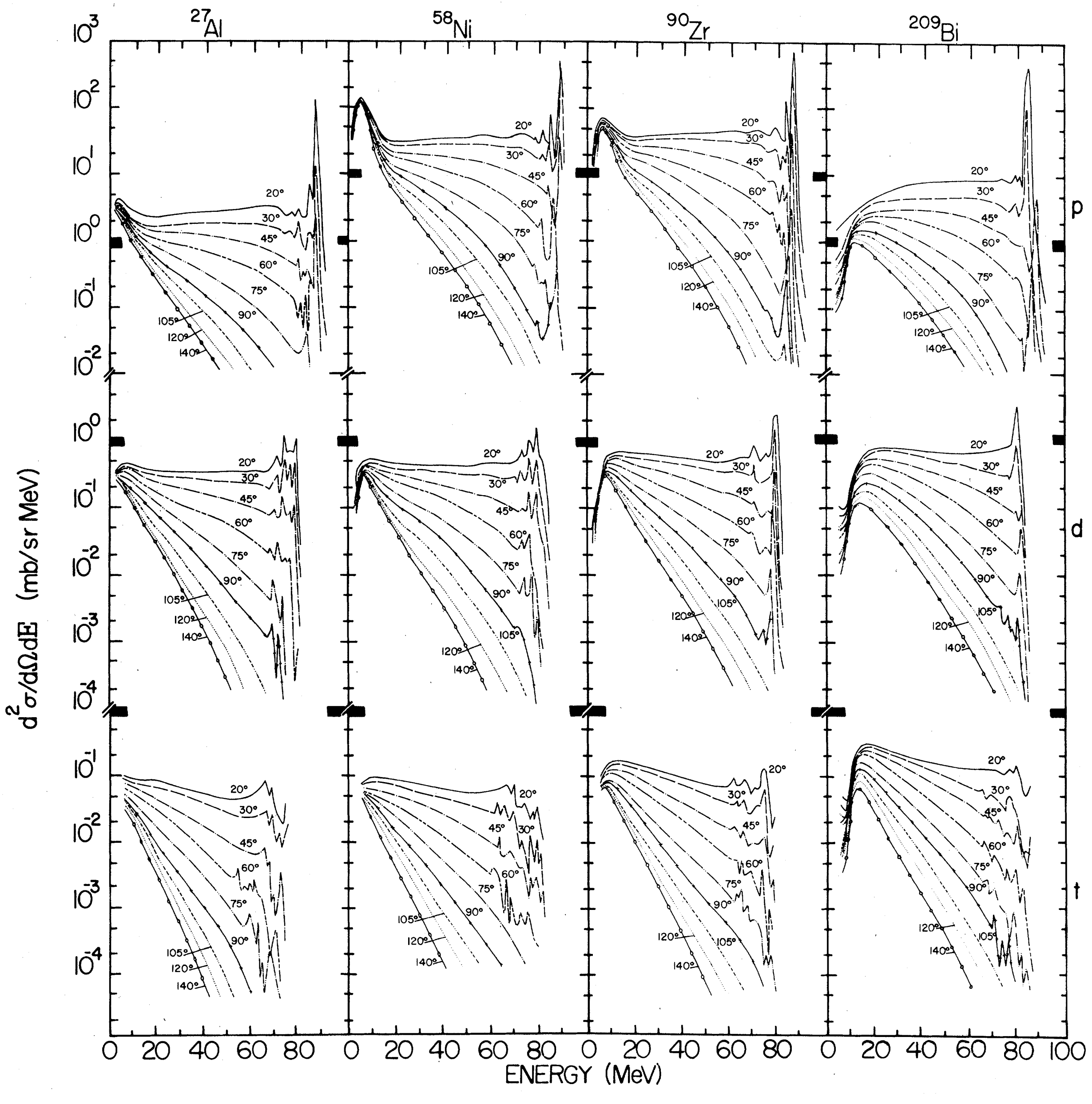

FIG. 1. The laboratory differential energy spectra for p, d, t, ^{3}He, and α particles resulting from the bombardment of 90 MeV protons on ^{27}Al, ^{58}Ni, ^{90}Zr, and ^{209}Bi. The heavy mark represents the cross section of 1 mb/sr/MeV.

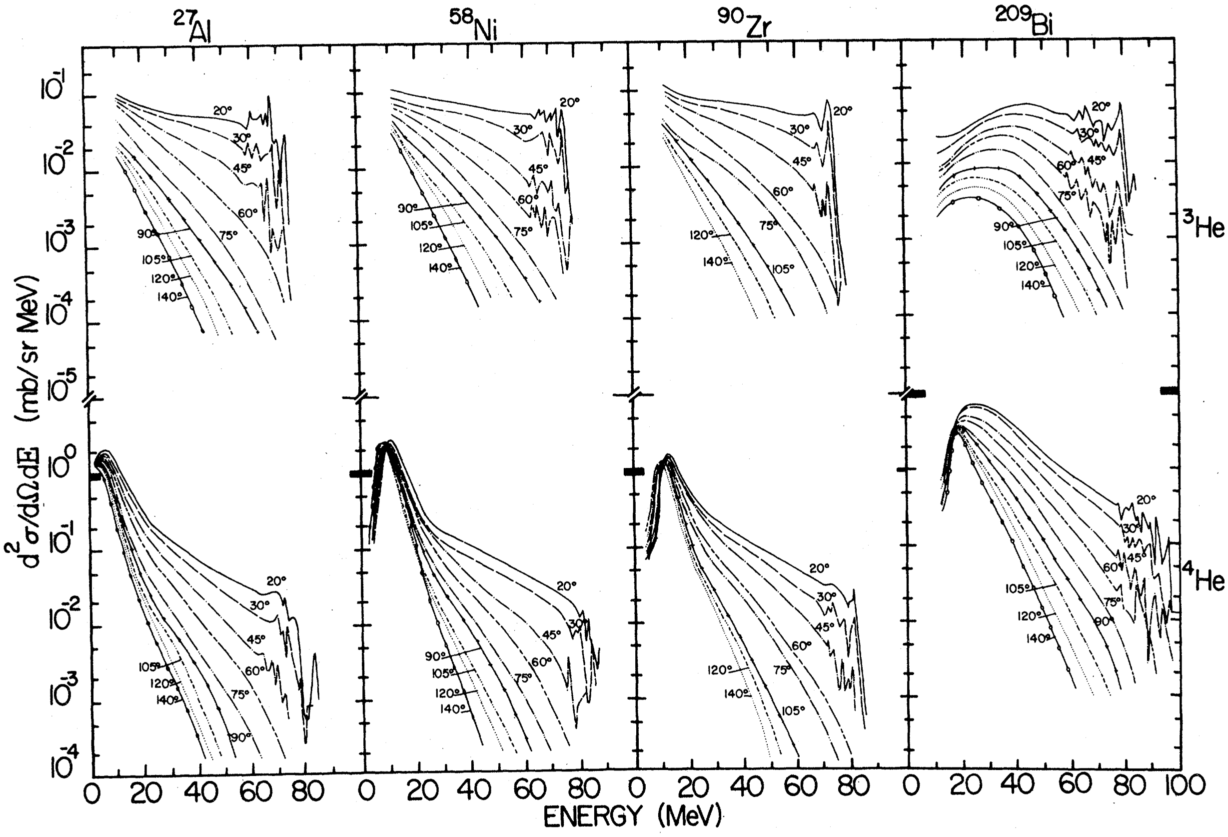

FIG. 1. (*Continued*).

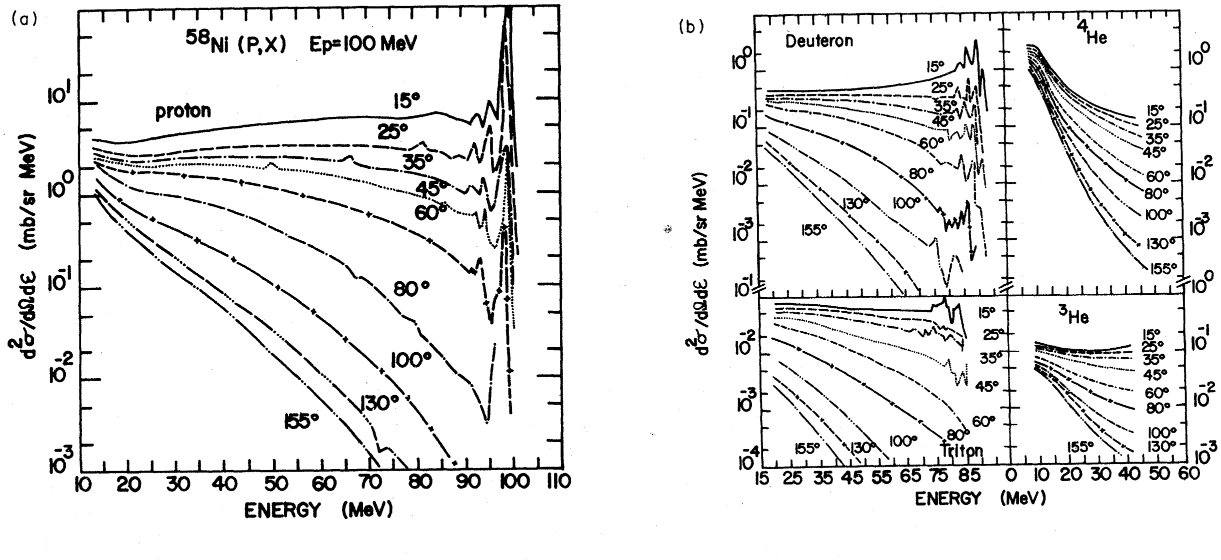

FIG. 2. (a) The laboratory differential energy spectra for protons resulting from the bombardment of 100 MeV protons on ^{58}Ni. 2(b) Same as Fig. 2(a) for d, t, ^{3}He, and α particles. Because of detector thickness used in the 100 MeV experiment. ^{3}He and α particles were measured over energy range from 8.5 to ~ 46 MeV.

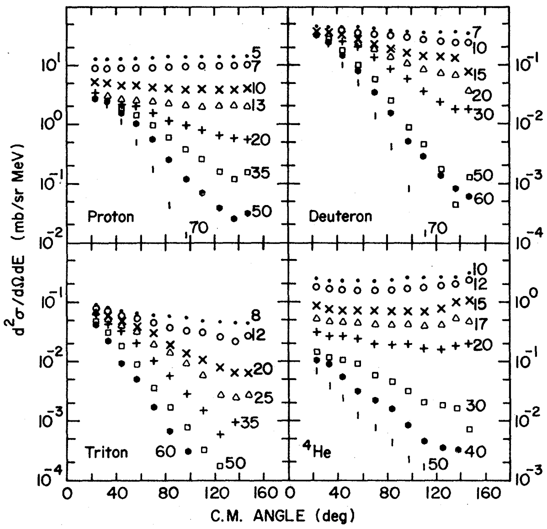

FIG. 3. Typical c.m. angular distributions for various energy bins (1 MeV bin) as indicated for the ^{58}Ni (p, x) reactions at $E_p = 90$ MeV.

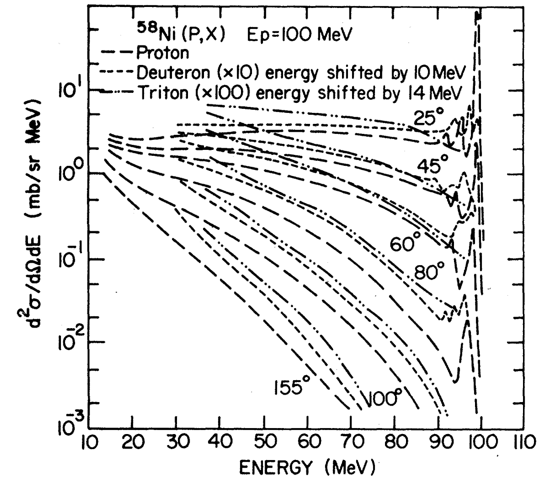

FIG. 5. Comparisons of proton, deuteron, and triton energy spectra for ^{58}Ni at $E_p = 100$ MeV. Deuteron and triton spectra have been shifted by an energy as indicated, and were scaled by a factor of 10 and 100, respectively.

ted protons. As previously indicated, an approximate $A^{1/3}$ dependence in the yield of nonequilibrium emission was observed at lower bombarding energies which suggests a peripheral type of reaction. The 90 MeV data shown in Fig. 7 [see also Fig. 9(c)] further support the previous observations for proton and deuteron emission. (The yield for ^{27}Al may deviate somewhat from the $A^{1/3}$ dependence.) Furthermore, the spectral shapes are very similar for all targets studied, except in the low-energy region. From the similarity in spectral shape and the $A^{1/3}$ dependence, we conclude that the reaction mechanisms involved in the emission of protons and deuterons are basically the same for all target nuclei.

Since the energy spectra are summed over approximately 1 MeV bins, the structure in the low-excitation region is smeared out. The cross section for these low lying states, however, constitutes only a small fraction of the total cross section. Figures 1 and 2 and Table III show how the charged light-particle yield is distributed among various energy regions and outgoing channels. The proton channel dominates in all cases. The non-

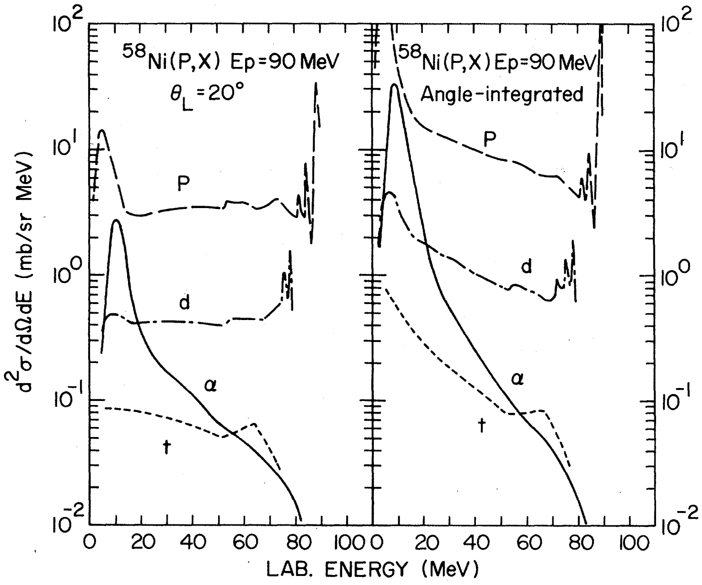

FIG. 4. Typical energy spectra at $\theta_L = 20°$ and the laboratory angle-integrated energy spectra for various emitted particles resulting from 90 MeV protons on ^{58}Ni.

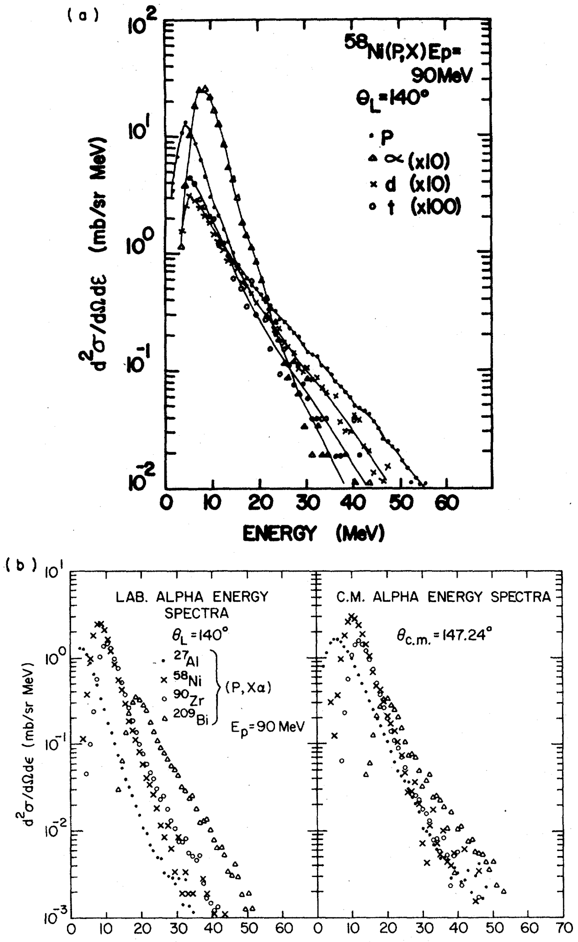

FIG. 6. (a) Typical laboratory energy spectra for the ^{58}Ni (p, x) reactions at $E_p = 90$ MeV and $\theta_L = 140°$. 6 (b) Laboratory and c.m. α particle energy spectra in the backward direction for various target nuclei at $E_p = 90$ MeV.

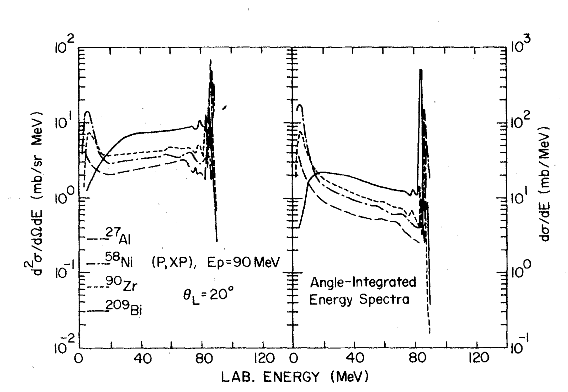

FIG. 7. Comparisons of charged light-particle spectra resulting from the bombardment of 90 MeV protons on various target nuclei at $\theta_L = 20°$ in the laboratory system.

equilibrium deuteron yield is roughly $\frac{1}{10}$ that of protons. The evaporation of protons and α particles is important for light and medium nuclei, but is unimportant for heavy nuclei. The equilibrium and nonequilibrium processes are comparable for light- and medium-mass nuclei, while the nonequilibrium process dominates the yield of charged light particles for heavy nuclei. (Clearly neutron evaporation and fission should be important for heavy nuclei.)

Figure 8 shows the laboratory energy-integrated angular distributions. The yields of all particles, except α particles, are strongly forward peaked and decrease smoothly as angle increases. The shapes of the angular distributions for a given nucleus are similar for all particles, except α-particles, and are more strongly forward peaked for the heavy nuclei than for lighter nuclei. The relatively flat angular distribution of α particles for the lighter nuclei suggests that the yield of α particles in the backward angles could result from evaporation. The strong forward peaking of the α particle yield for ^{209}Bi suggests that nonequilibrium processes are more important for α-particle emission from heavy nuclei.

In order to estimate the nonequilibrium cross section, we have first taken the spectrum at the most backward angle and multiplied by 4π to obtain the total evaporation yield. [A nonequilibrium component exists even at the most backward angle

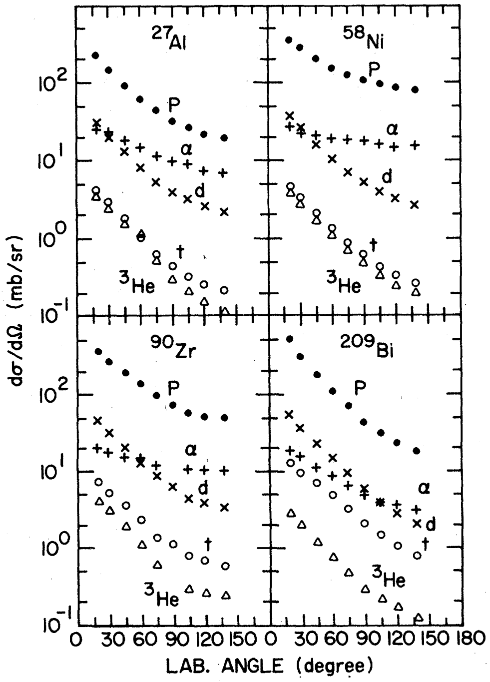

FIG. 8. The laboratory energy-integrated angular distributions for the ^{27}Al, ^{58}Ni, ^{90}Zr, ^{209}Bi (p,x) reactions at $E_p = 90$ MeV.

TABLE III. Summary of experimental results for 90 and 100 MeV proton induced reactions.

Target and incident energy	Emitted particle	Total integral cross section σ_β (mb)	σ_β/σ_t	Mean particle yield $Y_\beta=\sigma_\beta/\sigma_R$	MeV/ Reaction $=\bar{E}\times Y_\beta$	Discrete states cross section[b] (mb)	Evaporation cross section[c] $\sigma_{\text{eV (mb)}}$	Nonequilibrium cross section[d] $\sigma_{\text{neq (mb)}}$	Total mean particle yield $Y=\sigma_t/\sigma_R$
^{27}Al	p	723[a]	0.724	1.681	71.07	27[a]	256	440	
E_p=90 MeV	d	93	0.093	0.216	6.06	9	29	55	
	t	12	0.012	0.028	0.64	0.6	3	8.0	2.323
	^{3}He	10	0.010	0.023	0.67	0.4	1	8.6	
	^{4}He	161	0.161	0.374	3.18	0.1	90	70.9	
^{58}Ni	p	1794[a]	0.821	2.327	53.54	40[a]	1060	694	
E_p=90 MeV	d	118	0.054	0.153	4.79	12	35	71	
	t	14	0.006	0.018	0.47	0.7	3	10.3	2.835
	^{3}He	12	0.006	0.016	0.49	0.6	3	8.4	
	^{4}He	248	0.113	0.322	3.80	0.1	205	42.9	
^{90}Zr	p	1431[a]	0.809	1.329	41.89	53[a]	639	739	
E_p=90 MeV	d	144	0.081	0.134	4.20	13	43	88	
	t	24	0.014	0.022	0.54	0.9	7	16.1	1.642
	^{3}He	12	0.007	0.011	0.33	0.4	3	8.6	
	^{4}He	157	0.089	0.146	2.18	0.6	125	31.4	
^{209}Bi	p	1297[a]	0.817	0.708	41.23	58[a]	228	1011	
E_p=90 MeV	d	153	0.096	0.084	3.19	13	25	115	
	t	45	0.028	0.025	0.73	1.4	10	33.6	0.867
	^{3}He	8	0.005	0.004	0.17	0.4	2	5.6	
	^{4}He	85	0.054	0.046	1.32	0.1	39	45.9	
^{58}Ni	p	895[a]	0.791	1.161	⋯	45[a]	125	725	
E_p=100 MeV	d	85	0.075	0.110	⋯	10	6	69	
	t	9	0.008	0.012	⋯	0.7	0.3	8	1.462
	^{3}He	15	0.013	0.019	⋯	⋯	6	9	
	^{4}He	123	0.108	0.160	⋯	⋯	68	55	

[a] Elastic scattering peak is excluded.

[b] Discrete state cross sections are estimated by summing cross sections from 0–10 MeV in the low excitation region.

[c] Evaporation cross sections are estimated from the total cross section at 140° or 155° multiplied by 4π.

[d] Nonequilibrium cross sections are obtained by subtracting the evaporation and discrete state cross sections from the total integral cross section.

where the data were taken. However, this component is rather small (see Fig. 13). We have, therefore, assumed that the most backward angle spectrum could provide a reasonable estimation for the evaporation yield. This could over-estimate the evaporation cross section by not more than 20%.] The total evaporation yield was then subtracted from the angle-energy-integrated cross section to give the nonequilibrium cross section. Figure 9(a) shows the integral (angle and energy integrated) cross section for various charged light particles and the total charged light-particle integral cross section as a function of the target mass, *A*. Figure 9(b) shows the target mass dependence of the evaporation yield for each charged light particle and for the total evaporation yield. As can be seen from Figs. 9(a) and 9(b), the largest total charged light particle and evaporated yields occur around ^{58}Ni. This is also the case for the 62 MeV proton data (see Table II). The yield then decreases as *A* increases. This decrease may be due to the higher Coulomb barrier, which inhibits the evaporation of low-energy, charged light particles, and the strong competition of neutron emission (as

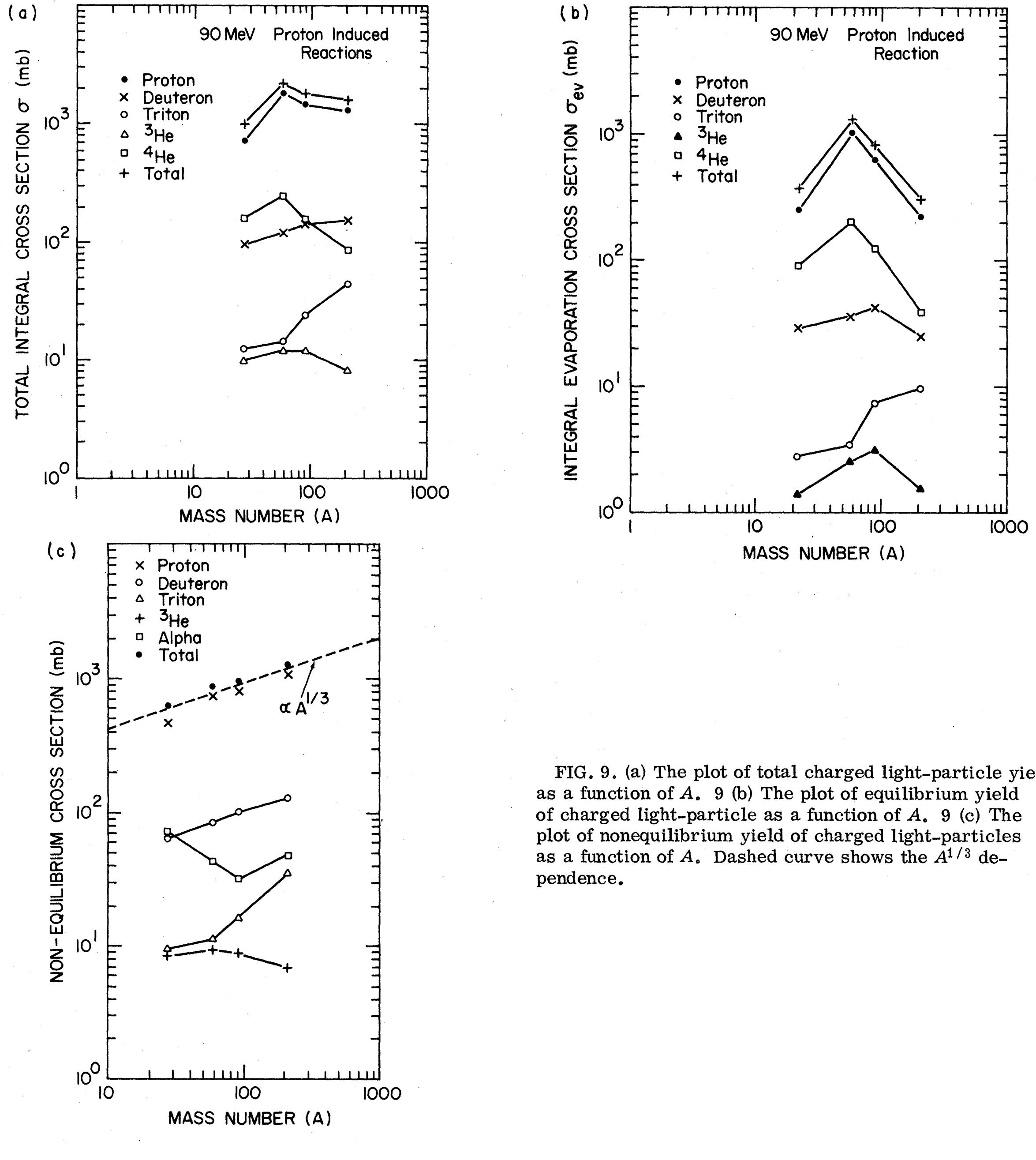

FIG. 9. (a) The plot of total charged light-particle yield as a function of *A*. 9 (b) The plot of equilibrium yield of charged light-particle as a function of *A*. 9 (c) The plot of nonequilibrium yield of charged light-particles as a function of *A*. Dashed curve shows the $A^{1/3}$ dependence.

well as fission for heavy nuclei). In Fig. 9(c) the nonequilibrium yield is plotted as a function of the target mass. The total nonequilibrium yield can be expressed as $(200 \pm 10)A^{1/3}$ mb. The total integral yield in the forward direction (< 90°) is ~ 70–90% of total charged light-particle yield. The total nonequilibrium charged light-particle yield is dominated by the proton and deuteron yields which have an approximate $A^{1/3}$ dependence. The triton yield shows a rapid increase with A; whereas the ^{3}He yield decreases with A. The yield of ^{3}He relative to that of tritons decreases rapidly as A increases. The decrease is considerably more rapid than the ratio of proton to neutron number as a function of A. The yield of tritons increases more rapidly than $A^{1/3}$, but the combined triton and ^{3}He yield increase approximately as $A^{1/3}$. The yields of tritons and ^{3}He may be due to peripheral reaction but they are influenced by the Coulomb barrier. The nonequilibrium yield of α particles does not appear to have a simple interpretation. The increase in the α-particle yield for heavy nuclei may be due to the binding energy effects. Table III summarizes the observed experimental results. As can be seen from Tables II and III, the dominant channel is the proton channel (60–90% of total charged light-particle yield). The fractions of individual charged light-particle yields (individual particle yield σ_β divided by the total charged light-particle yield, σ_t) for 90 MeV data are quite similar to those of 62 MeV protons.

It is interesting to note that the location of the low-energy evaporation peak shifts with angle. The shift is not as large as in the case of α particle or deuteron induced reactions.[1,2] It is, however, consistent with the two-body kinematics. Figure 10 shows that α-particle spectra at various angles in the initial c.m. frame. It is obvious that they are peaked at the same location. These observations imply that most of the evaporation yield results from complete momentum transfer processes.

Figure 11 shows linear plots of proton spectra at forward angles resulting from 90 and 100 MeV protons on ^{58}Ni. Broad peaks are clearly seen in these spectra at energies corresponding to quasifree scattering. The arrows in Fig. 11 indicate the expected quasifree peak locations as calculated from the three-body kinematics assuming zero recoil momentum. The sharp peaks are the free p-p scattering due to the hydrogen contaminant in the target. The quasifree peak is, however, not as distinct as in the higher energy studies.[4] It is interesting to note that the quasifree scattering peak is more pronounced at 100 MeV than at 90 MeV and is not evident at 62 MeV.[3] This may suggest that the distortion effects are important in this energy range.

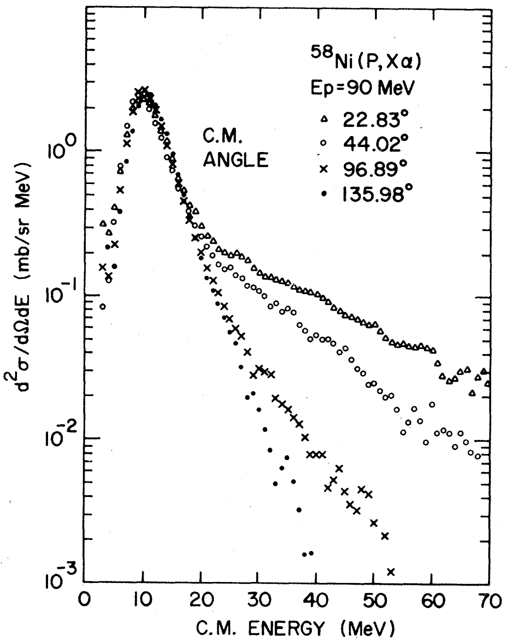

FIG. 10. The differential energy spectra for α particles at several angles in the c.m. frame resulting from the ^{58}Ni (p, x) reactions at $E_p = 90$ MeV.

The forward-angle proton spectra shown in Fig. 11 suggest that the quasifree scattering in which the incident nucleons interact with a single nucleon in the target nucleus is important. The struck nucleon can be ejected from the nucleus after the initial collisions or initiate a nuclear cascade through a series of nucleon-nucleon collisions.[10] During the cascade, particles could be ejected or the interactions could continue until an equilibrium state is reached. The protons emitted during the cascade contribute to the observed con-

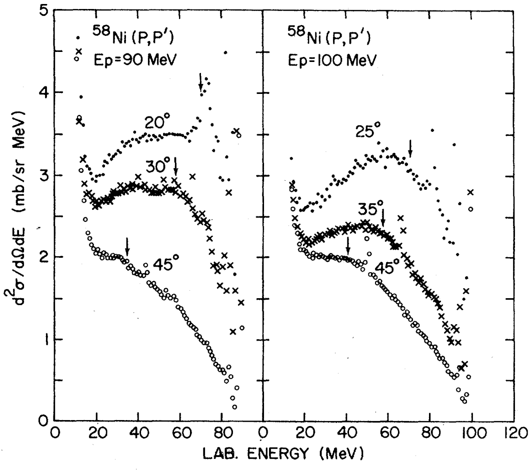

FIG. 11. The proton spectra resulting from 100 and 90 MeV protons on ^{58}Ni at several forward angles in the laboratory system. The arrows indicate the expected location of quasifree peak at various angles.

tinuum spectrum. The similarity between the deuteron (or triton) and the proton spectra in the high-energy continuum suggests that a similar reaction mechanism might be involved, i.e., before the cascade proton leaves the nucleus it picks up one (or two) neutron to form a deuteron (or triton).[11] The steeper slope for the triton spectra could be due to the fact that more interactions and greater momentum transfers are required to form a triton. Similarly, the production of ^{3}He particles could be interpreted as the successive pickup of two nucleons.

The emission of high-energy α particles could result either from the knockout of an α particle from the nuclear surface or the pickup of three nucleons. These two processes could in principle be distinguished on the bases of coincident experiments, such as the $(p, p\alpha)$ reactions.[12] Distortion effects not only severely reduce the knockout contribution in the observed spectrum of $(p, p\alpha)$ reactions, but also limit the observed contributions to the low-density region of the nuclear matter distributions. Such distortion effects would not be expected to be as severe in the single-particle spectra (where only one particle has to survive) and will have to be calculated before a comparison could be made between the two types of experiments.

In order to investigate the energy dependence of the production of charged light particles, and whether different mechanisms are involved in different energy regions, we have compared our data with the results of other authors obtained at lower energies. Spectra for ^{54}Fe(p, xp) at $E_p = 62$ MeV[3] and ^{58}Ni(p, xp) at $E_p = 90$ MeV are compared in Fig. 12. The data at these two energies exhibit the same general behavior. Similar behaviors are observed for other emitted particles. This observation suggests that the same basic reaction mechanisms are involved at both energies.

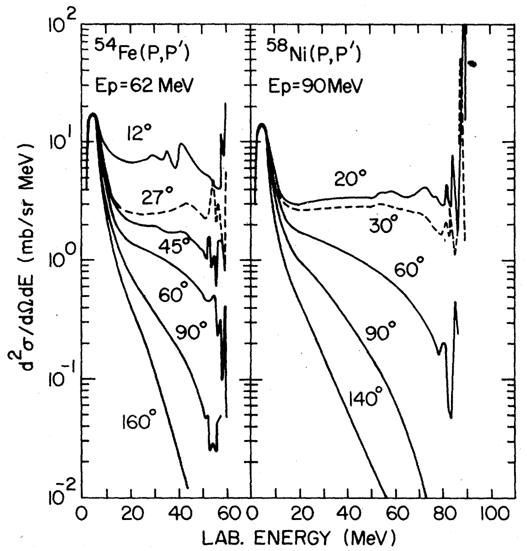

FIG. 12. Comparisons of the laboratory proton spectra resulting from 62 MeV protons on ^{54}Fe and 90 MeV protons on ^{58}Ni at various angles.

From the observed experimental results, the high-energy particles seem to "retain" much of the dynamic information of the incident particle and result in relatively small momentum transfers to the residual nucleus. The low-energy particles, which appear to be associated with processes involving large momentum transfers to the target system, do not "memorize" their original information and result from the statistically equilibrated nuclei.

IV. CALCULATIONS

The details of the reaction models used in this section have been described previously.[1,2,13,14] We will present here only the results of calculations. Moreover, we have restricted ourselves to the preequilibrium exciton model[8,13,14] and evaporation model calculations. The quantities needed in the calculations have been explained in Refs. 1, 13, and 14.

First, the evaporation calculation, as described in Ref. 13, was divided by 4π before comparing with the proton and α-particle spectra at backward angles in Fig. 13. In this calculation, the evaporation process continues until no energy is available for further evaporation. The level density of the form $\rho(E) \propto a^{-1/4}(E-\delta)^{-5/4}\exp[2a(E-\delta)]^{1/2}$ was used, where the level density parameter a is taken to be $A/8$ which is equivalent to a single-particle state density $g = 6a/\pi^2 = (3A/4\pi^2)$ MeV^{-1}, and δ is the pairing energy. All calculated cross sections are absolute in magnitude, and the total reaction cross sections σ_R needed in the calculation were

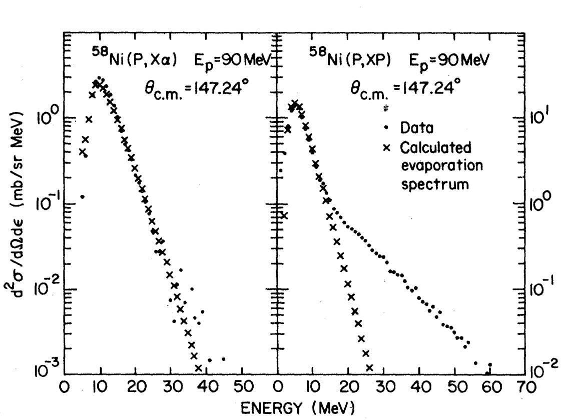

FIG. 13. Comparisons of calculated evaporation spectra with experimental proton and α particle spectra at $\theta_{c.m.} = 147.24°$ in the c.m. frame for the ^{58}Ni (p, x) reactions at $E_p = 90$ MeV.

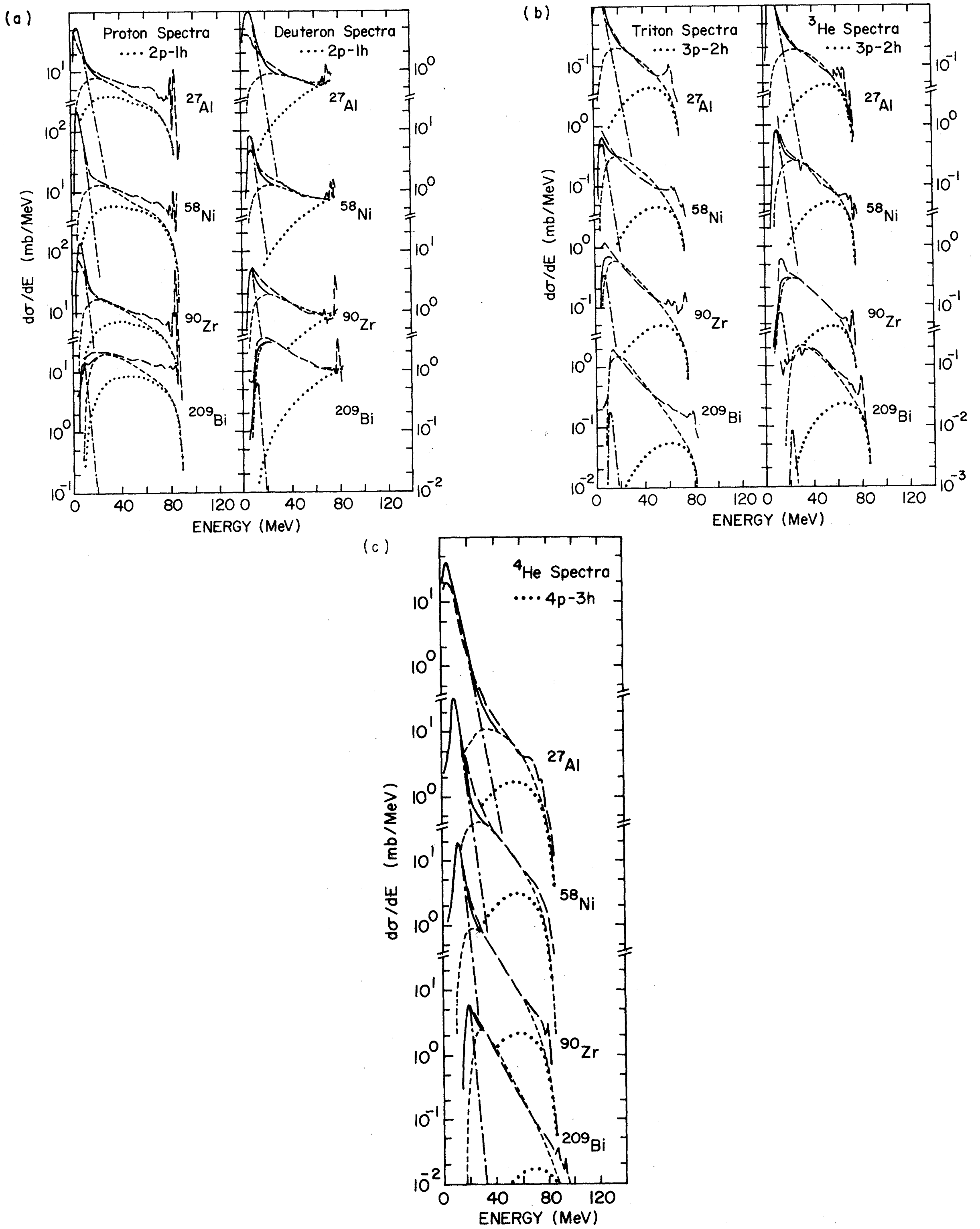

FIG. 14. (a) Comparisions of calculated spectra with experimental angle-integrated energy spectra of protons and deuterons for 90 MeV protons on ^{27}Al, ^{58}Ni, ^{90}Zr, and ^{209}Bi. — — data; ··· calculated preequilibrium spectra resulting from the first stage as indicated; --- calculated total preequilibrium spectra; -∘-· calculated evaporation spectra; and — calculated total spectra (sum of the total preequilibrium and evaporation spectra). The initial particle-hole number is 2p-1h. 14 (b) Same as Fig. 14 (a) except for tritons and ^{3}He. 14 (c) Same as Fig. 14 (a), except for ^{4}He.

taken from Ref. 15. The evaporation calculation gives a rather good description of the major component of the particles emitted in the backward direction, although a small nonevaporation component exists for protons.

Figure 14 shows comparisons of experimental angle-integrated energy spectra with calculations for all target nuclei studied. For the preequilibrium exciton model calculation, an initial particle-hole configuration of 2p-1h (an initial exciton number equal to 3) is used for proton induced reactions. The average two-body transition matrix elements $|M|^2$ are given by the empirical expression, $|M|^2 = KE^{-1}A^{-3}$ with $K = 200$ MeV^3.[16] It should be pointed out that no multiparticle emission was included in the preequilibrium emission. The secondary preequilibrium emission is treated as an evaporation process for simplicity.

The spectra resulting from the first stage preequilibrium emission (p and d from 2p-1h, t and ^{3}He from 3p-2h, and α particle from 4p-2h) are shown as dots in Fig. 14. This contribution accounts for most of the high-energy yield of protons and a good part of the highest energy nonequilibrium yield of other particles. In the case of proton emission, the first stage (2p-1h states) contribution is somewhat equivalent to the quasifree scattering. The average energy of protons emitted from this state is $\sim \frac{1}{2}$ of the initial excitation energy. The short dashed curves in Fig. 14 are the calculated total preequilibrium spectra which are the sum of particle emission from all of the preequilibrium stages. The calculated evaporation component and the total calculated spectra (the sum of total preequilibrium and evaporation calculations) are shown in Fig. 14 as dash-dotted and solid curves, respectively.

The emission of complex-particles such as deuterons results from nucleon-nucleon interactions followed by nucleon pickup (or from the cascade nucleon subsequently picking up another nucleon). By normalizing the calculation for complex particles to the experimental data at the high-energy end of the spectra, the complex-particle formation probability, as described in Ref. 14 can be extracted. This complex-particle formation probability represents the probability of the cascade nucleon picking up one or more nucleons with proper momenta to form the observed particle. The complex-particle formation probabilities γ_β extracted from this procedure are given in Table IV. The values of γ_β's depend strongly on the choice of σ_R, the

TABLE IV. Summary of calculated results.

Target and incident energy	Total reaction cross section σ_R (mb)	Initial particle and hole number	Emitted particle	Measured nonequilibrium yield (mb)	Complex particle formation probability $\gamma_\beta g/g_\beta$		Calculated preequilibrium yield	
					No pairing correction	Pairing correction	Total (mb)	First stage (mb)
^{27}Al			p	440	...	...	248	154
E_p= 90 MeV	430	2p-1h	d	55	0.0364	0.0331	51	22
			t	8.4	0.0147	0.0165	7	2
			^{3}He	8.6	0.0083	0.0091	7	2
			^{4}He	70.9	0.0092	0.0201	39	7
^{58}Ni			p	694	...	...	480	267
E_p= 90 MeV	770	2p-1h	d	71	0.0273	0.0268	70	25
			t	10.3	0.0085	0.0092	11	2
			^{3}He	8.4	0.0056	0.0049	9	2
			^{4}He	42.9	0.0099	0.0093	13	1
^{90}Zr			p	739	...	...	615	319
E_p= 90 MeV	1077	2p-1h	d	88	0.0255	0.0255	95	29
			t	16.1	0.0055	0.0066	18	2
			^{3}He	8.6	0.0037	0.0033	10	2
			^{4}He	31.4	0.0045	0.0046	22	1
^{209}Bi			p	1011	...	...	757	385
E_p=90 MeV	1831	2p-1h	d	115	0.0196	0.0186	134	31
			t	33.6	0.0034	0.0033	40	2
			^{3}He	5.6	0.0013	0.0013	7	1
			^{4}He	45.9	0.0017	0.0020	49	1
^{58}Ni			p	725	...	...	462	263
E_p=100 MeV	771	2p-1h	d	69	0.0271	...	67	25
			t	8	0.0071	...	6	2
			^{3}He	9	...	...	7	1
			^{4}He	55	...	...	8	2

total reaction cross section (see also Ref. 14). Figure 15 shows the log-log plot of $\gamma_\beta g/g_\beta$ as a function of A. A strong A dependence of $\gamma_\beta g/g_\beta$ is found for each particle. Similar A dependence was also observed for reactions induced by 80 MeV deuterons,[1] 140 MeV α particles,[2] and lower energy protons (< 62 MeV).[14] A family of curves corresponding to various A dependence are also shown. It should be noted that the pairing effect tends to play an important role in extracting the values of γ_β. The effect can be seen in Fig. 15. (See Ref. 14 for more detailed discussions.)

The calculations generally reproduce the experimental spectra reasonably well in shape, but underestimate the proton yield in the region of high-energy continuums. If the reaction cross sections used in our calculations[15] are too small, this discrepancy could be accounted for. A change in the magnitude of the reaction cross section would affect the complex-particle energy spectra, but the magnitudes of the complex-particle energy spectra could be corrected by varying the complex-particle formation probability. The overall agreement between the calculations and the experimental spectral shape is encouraging.

Because of the limitation of the preequilibrium exciton model used in this paper, no calculations of the experimental angular distributions were possible. Some preequilibrium models have been recently developed to account for the angular distributions.[17] So far, however, they are limited to nucleon channels and lower energies only. As in our previous studies, the complex-particle channels are very important and constitute a large fraction of the total charged light-particle yields (~ 20%). One is not justified in neglecting their competitions in any model calculation.

V. CONCLUSION

To summarize this work, we list briefly the main experimental observations as follows:

(1) The spectra of each emitted charged light particle has a characteristic behavior with angle which is similar for all target nuclei except in the low-energy evaporation region.

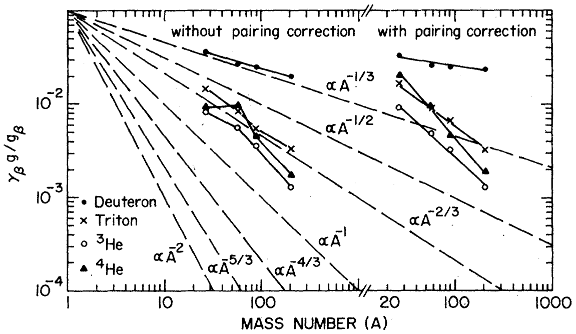

FIG. 15. Plot of $\gamma_\beta\, g/g_\beta$ as a function of A. Dashed lines show various A dependence.

(2) The dominant reaction channel is the proton channel which accounts for about 80% of total charged light-particle yield.

(3) Excluding the elastic peak, low-lying discrete states ($E_x \lesssim 10$ MeV) account for only $\lesssim 5\%$ of total charged light-particle yield.

(4) The total nonequilibrium yield of charged light particles can be expressed as $(200 \pm 10)A^{1/3}$ mb. The approximate $A^{1/3}$ dependence seems to suggest that the nonequilibrium yield is due primarily to peripheral processes. From the magnitude of the nonequilibrium yield one could conclude that more than one particle is emitted from such peripheral processes, for example, the quasifree $(p, 2p)$ and (p, pn) reactions.

(5) The high-energy continuums of the spectra show a strong angular dependence in the forward direction suggesting that this region is dominated by relatively direct interactions. The proton and α-particle spectra in the backward directions and at low energies are nearly isotropic especially for lighter nuclei, which indicates that this region is dominated by an equilibrium process.

(6) The shape and magnitude of spectra above the low-energy evaporation peak vary with the emitted particle type. The yield decreases in the order of p, d, t, (^{3}He), and α particle with the ratio of the $p/d/t$ yields approximately 100/10/1, respectively. The shapes of deuteron spectra are very similar to those of protons if they are shifted by about 10 MeV, the binding energy difference of the picked up neutron. Even the triton spectra are very similar to the proton spectra, if they are shifted by approximately 14 MeV.

(7) The evaporation process is comparable to the nonequilibrium process for medium and light nuclei, but the latter becomes dominant for the heavy nuclei, where neutron emission and fission compete strongly with charged light-particle evaporation.

(8) The quasifree scattering peak is evident in the forward angle proton spectra but it is not as striking as in higher energy data.[4]

(9) The total charged light-particle yield is about a factor of 2 larger than the total reaction cross section (σ_R) for medium and light nuclei, and is roughly 0.9 of σ_R for heavy nuclei. As neutron emission and fission are very important for heavy nuclei, multiparticle emission processes are necessary in order to produce the observed yields of particles.

As shown in Sec. IV, the model calculations are limited only to the angle-integrated energy spectra. A more sophisticated model is needed to account for both angular distributions and complex-particle spectrum.[18] Even though a number of simplifications have been made on the present calculations, the angle-integrated data reported here are reasonably well described by the preequilibrium exciton and compound nuclear evaporation models. A single scattering process which is equivalent to the first stage of the preequilibrium spectrum is unable to predict the entire energy spectra. Such a process, however, accounts for a large fraction of the nonequilibrium proton yield and most of high-energy deuterons. On the other hand, the comparison of the experimental results with the calculations indicate that multiple collisions are significant at this energy range, particularly for complex-particle emission.

ACKNOWLEDGMENTS

The authors would like to thank the operating staff of the University of Maryland Cyclotron. We would also like to thank T. Carey, M. Collins, M. Glascock, and C. Wang for the help in data taking. A grant from the University of Maryland Computer Science Center for carrying out these calculations is acknowledged. This work was supported in part by the National Science Foundation.

---

[1] J. R. Wu, C. C. Chang and H. D. Holmgren, Phys. Rev. C (to be published).

[2] J. R. Wu, C. C. Chang and H. D. Holmgren, Phys. Rev. C (to be published).

[3] F. E. Bertrand and R. W. Peelle, Phys. Rev. C 8, 1045 (1973); ORNL Reports Nos.: ORNL-4450, 1969; ORNL-4455, 1967; ORNL-4460, 1969; ORNL-4469, 1970; ORNL-4471, 1970; ORNL-4638, 1971; ORNL-4799, 1973 (unpublished).

[4] P. G. Roos and N. S. Wall, Phys. Rev. 140, B 1237 (1965); N. S. Wall and P. G. Roos, *ibid.* 150, 811 (1966); J. B. Cladis *et al.*, *ibid.* 87, 425 (1952); J. W. Wachter *et al.*, Phys. Rev. C 6, 1496 (1972); L. S. Azhgirey *et al.*, Nucl. Phys. 13, 258 (1958); D. M. Corley *et al.*, *ibid.* A184, 437 (1972).

[5] R. K. Bhowmik, C. C. Chang, J.-P. Didelez, and H. D. Holmgren, Phys. Rev. C 13, 2105 (1976); P. G. Roos, N. S. Chant, A. A. Cowley, D. A. Goldberg, H. D. Holmgren, and R. Woody, III, *ibid.* 15, 69 (1977); A. A. Cowley, P. G. Roos, N. S. Chant, R. Woody, III, H. D. Holmgren, and D. A. Goldberg, *ibid.* 15, 1650 (1977).

[6] C. C. Chang, N. S. Wall, and Z. Fraenkel, Phys. Rev. Lett. 33, 1493 (1974).

[7] J. R. Wu *et al.*, in Proceedings of the 2nd International Conference on Clustering Phenonmena in Nuclei, College Park, Maryland, 1975, edited by D. A. Goldberg (unpublished).

[8] C. K. Cline, Nucl. Phys. A193, 417 (1972); H. W. Bertini, G. D. Harp, and F. E. Bertrand, Phys. Rev. C 10, 2472 (1974), and references therein.

[9] J. R. Wu, Ph.D. thesis, University of Maryland, 1977 (unpublished).

[10] M. L. Goldberger, Phys. Rev. 74, 1289 (1948); N. Metropolis *et al.*, *ibid.* 110, 185 (1958); 110, 204 (1958); H. W. Bertini *ibid.* 131, 1801 (1963); K. Chen *et al.*, Phys. Rev. C 4, 2234 (1971).

[11] B. H. Bransden, Proc. Phys. Soc. London A65, 738 (1952); S. T. Butler and C. A. Pearson, Phys. Rev. Lett. 7, 69 (1961); 1, 77 (1962); Phys. Rev. 129, 836 (1963); Phys. Lett. 9, 330 (1964).

[12] N. S. Chant, H. D. Holmgren, and P. G. Roos, Univ. of Maryland Technical Report No. 78-017, 1977 (unpublished).

[13] J. R. Wu and C. C. Chang, Phys. Rev. C 16, 1812 (1977), and references therein.

[14] J. R. Wu and C. C. Chang, Phys. Rev. C 17, 1540 (1978), and references therein.

[15] P. Kirkby and W. T. Link, Can. J. Phys. 44, 1847 (1966); K. Kwiatkowski, Ph.D. thesis, University of Maryland, 1976 (unpublished); A. Nadasen, Ph.D. thesis, Indiana University, 1977 (unpublished).

[16] C. K. Cline, Nucl. Phys. A210, 590 (1973).

[17] G. Mantzouranis *et al.*, Phys. Lett. 57B, 220 (1975); G. Mantzouranis, Phys. Rev. C 14, 2018 (1976); Y. Ivie *et al.*, Phys. Lett. 62B, 9 (1976).

[18] T. Tamura and T. Udagawa, Phys. Lett. 71B, 273 (1977).